Mixed Molybdenum-Tungsten Oxide as Dual-Band, VIS-NIR Selective Electrochromic Material

Authors: F. Gillissen[1], M. Lobet[2], J. Dewalque[1], P. Colson[1], G. Spronck[1], R. Gouttebaron[2], M. Duttine[3], B. Faceira[3], A. Rougier[3], L. Henrard[2], R. Cloots[1,], A. Maho[1,3,*]*

[1] Group for Research in Energy and Environment from Materials (GREEnMat), University of Liège, Quartier Agora – B6a, Allée du Six-Août 13, 4000, Liège, Belgium.

[2] Department of Physics, Namur Institute of Structured Matter, University of Namur, Rue de Bruxelles 51, 5000, Namur, Belgium.

[3] University of Bordeaux, CNRS, Bordeaux INP, ICMCB, UMR 5026, 87 Avenue du Dr Albert Schweitzer, F-33600, Pessac, France.

* Corresponding authors: rcloots@uliege.be, anthony.maho@icmcb.cnrs.fr

Keywords

Electrochromism, smart windows, energy-efficient buildings, metal oxides; solvothermal synthesis; thin films; wet coating.

Abstract

Energy efficiency of smart windows can be greatly improved by integrating dual-band electrochromic materials based on nanostructured doped metal oxides, as these will allow for a dynamic and independent control of light and heat supplies in buildings respectively related to transmitted visible (VIS) and near-infrared (NIR) solar radiations. Mixed molybdenum – tungsten oxides $Mo_yW_{1-y}O_{3-\delta}$ "MoWOx" are considered as innovative compounds in this context: in comparison with parent $WO_{3-\delta}$ formulations, a remarkable increase of unpaired electrons can be obtained from the formation of a larger amount of both reduced species and oxygen vacancies during the synthetic process of MoWOx materials, with a consequently boosted intensity of light absorption by 850-900 nm wavelengths. Consecutively, spin-coated films obtained from MoWOx structures solvothermally synthesized for 1h from 2/1 Mo/W atomic ratios are shown to be electrochromically commutable through a noticeable VIS-darkened and NIR-transparent *warm* mode, while $WO_{3-\delta}$ benchmarks classically evolve between *bright* (VIS & NIR bleached), *cool* (VIS-bleached, NIR-opaque) and *dark* (VIS & NIR opaque) states. All in all, such advanced optical functionalities are of high interest for fine-tuning the selectivity and improving the efficiency of electrochromic fenestration solutions, further improving their capacity to adapt to different climates, seasons, and users preferences.

1. Introduction

Nanostructured heavily doped semi-conductors testify for near-infrared (NIR) optical absorption through localized surface plasmon resonance (LSPR) phenomena, in which the free charge carriers collectively oscillate upon interaction with incident electromagnetic radiation.[1–3] The plasma frequency ω_p of the materials depends directly on the quantity of these free charge carriers, as well as on other parameters such as the particle size, shape, composition and environment.[1,4] Therefore, their optical absorption can be tuned by varying the free charge carrier concentration between values of 10^{19} to 10^{21} cm^{-3}, specifically by the means of synthetic doping. Different strategies have been accordingly developed to tune the optical response in tungsten oxide (WO_3) based compounds, including the formation of bronzes by heteroatom-doping with Li, Na, K, Rb, Cs…,[5–7] or by the creation of oxygen vacancies, and therefore of substoichiometric $WO_{3-\delta}$ formulations, especially by means of solvothermal treatment[8–13] or synthesis under controlled atmosphere (typically using Schlenk line setups).[14–16]

Given their capacity to selectively modulate NIR light absorption, such electronically tunable nanomaterials are highly interesting for electrochromic applications, in which optical modulation is controlled *post-synthesis* by applying an appropriate electrochemical bias.[1] Typically, $WO_{3-\delta}$ compounds have been explored to induce an electrochromic behavior in the 800-1300 nm region, which accounts for nearly half of the infrared intensity of an incoming solar source.[2,4] The origin of this absorption at energies much smaller than the band gap is still questioned, but often associated with the additional electrons brought either by the ionization of the dopant species or liberated during the formation of oxygen vacancies.

According to various authors, NIR optical properties of the then-created degenerate semiconductor nanocrystals are ruled by the free electron density in the conduction bands and the associated LSPR resonance, while the visible (VIS) response is driven by polaronic phenomena and responsible for its "conventional" electrochromism.[4,17] On one hand, if the additional electrons are not associated to electronic states localized near vacancies of energies lying within the band gap, they are delocalized into the conduction band of the oxide, without reduction of the transition metal atoms;[18] consequently, a plasmonic optical response is expected in the case of nanocrystalline compounds. On the other hand, if the newly added electrons occupy localized states having energies within the band gap, the W atoms are partly reduced to W^{5+}, as reported in literature from XPS measurements,[19,20] and therefore no plasmonic response is expected. The latter situation is often referred to as a polaronic effect, even though it is rather similar to a color center phenomenon,[21] which is different from the polaron met in the trivalent oxides – nevertheless, this terminology used in the present study so to be consistent with the literature. It has been also shown that, upon further doping by alkali atoms, the extra electrons occupy states localized on the vacancy sites,[22] in line with the polaronic hypothesis. The absence of a consensus on this matter is also due to the numerous crystalline phases of the considered nanocrystals, highly depending on the synthesis conditions and on the charge states.[23] Indeed, the vacancy states have been shown to depend on the phase and, for each phase, on the crystallographic site of the missing oxygen atoms. Up to now, simulations have not been conclusive on the role of the vacancy states because of the strong dependence of the results on the functional in DFT calculations.[24]

Beyond this ongoing debate on the fundamentals of their optoelectronic behavior, these semiconducting materials have thus a concrete applied use in allowing a so-called dual-band VIS-NIR electrochromic modulation behavior,[1,2,4,17] in which three states of optical filtration are generally available: the conventional *bright* and *dark* states (respectively transparent and opaque in both VIS and NIR), and an intermediate, NIR-selective, *cool* state (VIS-transparent and NIR-dark).[2] Therefore,

electrochromic fenestration solutions being designed and operated upon this dual-band system could improve the energy efficiency of smart windows and exceed the energy savings already reached by conventional electrochromic technology,[25,26] owing to a more efficient, selective control over the transmitted visible (luminosity) and NIR (heat) contributions of the solar radiation in buildings.

Even though dual-band materials offer an innovative functionality in comparison to their conventional counterparts, they still suffer from some limitations preventing them from large scale production and widespread implementation. Solutions as to circumvent these issues have been proposed in previous works of the literature, amongst those: the improvement of their selectivity towards the VIS and NIR ranges,[27,28] the development of suitable counter electrodes to improve the selectivity and efficiency of electrochromic devices,[1,17] the use of conductive substrates with broadband transparency as not to impair with the electrochromic behavior of the material (particularly in the NIR),[17] as well as the getting of a fourth, *warm* filtration mode (VIS-dark and NIR-transparent) so to further improve the functionality and efficiency of the devices.[27–31]

In a will to optimize the degree of NIR/VIS selectivity in tungsten oxide based electrochromic materials, the molybdenum – tungsten mixed oxides have been identified as interesting candidates. The association of molybdenum with (stoichiometric) WO_3 compounds has already been reported to improve their conventional (*i.e.* non-plasmonic) electrochromic performances by improving the color efficiency, the contrast between optical states, the stability, reversibility and durability of the material or by yielding a more neutral color in the dark state.[32,33,42–45,34–41] However, to this day, none of these studies have highlighted neither NIR-selective behavior nor dual-band functionality from these formulations. On the other hand, the concomitant formation of the mixed oxide as well as oxygen vacancies could lead to a further increased concentration of free charge carriers, being necessary to support LSPR features and to display a dual-band electrochromic behavior. As a matter of facts, several works have already highlighted the occurrence of a plasmonic behavior in such oxygen-deficient molybdenum – tungsten mixed oxides,[8–12,46–48] showing a large increase in their optical signal in comparison to the $MoO_{3-\delta}$ and $WO_{3-\delta}$ parent formulations, and accounting for a 15 and 20 times increase in absorption, respectively.[8] However, the current state-of-the-art focusing on these molybdenum – tungsten mixed oxides has only addressed (photo)catalytic applications so far. In the perspective of designing novel electrochromic materials, the combination of both oxygen vacancy doping (to allow the support of plasmonic features) and molybdenum incorporation (to improve the VIS electrochromic performances of WO_3) also bears great potential for enhancing the selective modulation of VIS and NIR ranges, as shown hereafter.

The present contribution aims at an efficient synthesis of suitable mixed Mo-W oxide formulations, further labeled as “MoWOx”, and at their film deposition through wet coating approaches. The impact of the oxide mixing on the morphological, crystalline and more importantly optical and electronic properties of the materials is carefully investigated in order to assess their potential as dual-band electrochromic material, specifically in terms of VIS/NIR selectivity, coloration and bleaching behavior, and reversibility.

2. Results

2.1. Solvothermally-synthesized "MoWOx" and $WO_{3-\delta}$ powders

2.1.1. Preliminary rationalization of the synthetic parameters: Mo/W stoichiometry and duration of the solvothermal process

Different formulations of MoWOx mixed oxides have been synthesized through a one-step solvothermal process on the basis of a reported protocol.[8] As starting compounds, three Mo/W molar ratios (2/1, 1/1 and 1/2) are selected while other synthetic parameters are maintained identical, *i.e.* a 160°C temperature and a 12h duration.

Optical measurements in non-diluted conditions (**Figure S1**), reproducing previous literature,[8,10,46,47] as well as in 10 wt. % diluted conditions (cf. inset in Figure S1) in order to meet the requirements of the KM formalism[48] (cf. Materials and Methods), show that the MoWOx 2/1 sample presents the most intense absorption properties out of the three ratios. Displaying a maximum at the beginning of the NIR, namely in the 800-1300 nm range where most of the NIR solar radiative intensity is found, this particular MoWOx formulation confirms its interesting potential as dual-band, VIS *and* NIR active electrochromic material. The remainder of this work will therefore focus on the investigation of this formulation and the characterization of its properties.

The impact of synthesis duration is then investigated, probing the evolution of the morphological, structural, optical and electronic properties of the material as the particles grow in the solvothermal reactor, with syntheses carried out during 1 to 12h. For all durations, urchin-like particles are obtained with a solid core covered by an outer layer of nanorods, growing from an average of 1.5 ± 0.5 µm at 1h to 2.6 ± 0.6 µm after 3h and up to 12h (**Figure S2**). As the urchin-like MoWOx particles do not grow further after 3h of solvothermal treatment, only the two limit durations of 1h and 12h (the latter also being the duration studied in previous works of the literature[8,9,12,47]) are considered for the next sections of this paper. In addition to the two MoWOx formulations (2/1, 1h and 12h), two $WO_{3-\delta}$ parent oxides produced following the same synthetic protocols (160°C, 1h and 12h) are also considered as benchmark formulations, and accordingly synthesized and characterized. The samples obtained from the solvothermal process exhibit different colorations (see pictures shown in **Figure S3**), notably: a dark blue tint in the case of both 1h and 12h MoWOx formulations, while the $WO_{3-\delta}$ parent oxides display lighter colors, with the "1h" sample leaning towards a grey/green color and its 12h counterpart being recovered as a light grey powder. Noteworthy, parent $MoO_{3-\delta}$ formulations are not considered in the present study, as preliminary trials have shown that the obtained particles were not stable enough to be processed as suspensions for thin film deposition, forming a thick slurry unable to be deposited by spin coating when prepared in the same conditions as the other formulations (125 mg/mL in ethanol, see Materials and Methods).

2.1.2. Morphological and structural analysis of "MoWOx" 2/1 and $WO_{3-\delta}$ powders

TEM micrographs of the four formulations of interest are presented in **Figure 1**, displaying very different morphologies. In the case of the MoWOx particles, both formulations highlight an urchin-like morphology, with the 1h formulation (Figure 1a, 1.5 ± 0.5 µm) growing into its larger 12h counterpart (Figure 1b, 2.6 ± 0.6 µm). However, due to the dense packing of nanorods at the surface of the urchins, the core-to-nanorods ratio could not be monitored nor tuned as a function of the time under solvothermal treatment from these measurements. For the parent $WO_{3-\delta}$ formulations, the morphology varies significantly as a function of the time, evolving from very aggregated nanospheres

(6.4 ± 1.6 nm) in the case of $WO_{3-\delta}$ 1h (Figure 1c), to micrometric hexagonal platelets (L x W x H = 1.9 x 1.9 x 0.2 µm (± 0.4 x 0.1 x 0.1 µm)) after 12h of solvothermal treatment (Figure 1d). Importantly, the nanostructures found in these materials – *i.e.* either the nanospheres (Figure 1c), the nanometric thickness of the hexagonal platelets (Figure 1d), or the nanorods at the surface of the urchins (Figure 1a,b) – could allow the support of plasmonic features in these formulations.

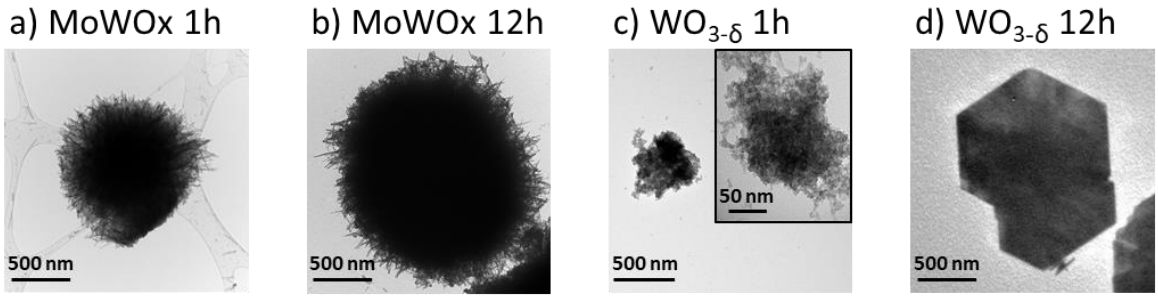

Figure 1: TEM micrographs of particles of (a) MoWOx 1h, (b) MoWOx 12h, (c) $WO_{3-\delta}$ 1h (with a greater magnification on an aggregate in inset), and (d) $WO_{3-\delta}$ 12h.

Complementary EDX characterization of the MoWOx powders (achieved in the SEM experimental setup, see Figure S2) highlights a disparity in the Mo/W ratios, with a molybdenum rich oxide for short-duration synthesis (Mo/W = 5/1 for the 1h case), followed by a decrease in the relative Mo content over longer durations (3h and more) to finally attain the targeted ratio of 2/1 (the initial ratio of the precursors in the reactive medium, see Materials and Methods). These results tend to indicate faster reaction kinetics for the molybdenum species in comparison to the tungsten ones, leading first to the formation of Mo-rich particles, to which the remaining dissolved tungsten incorporates over the next hours of reaction, until the reactive medium is completely depleted from metallic precursors.

XRD characterization of the MoWOx powders (**Figure 2**) exhibits only two diffraction peaks at 22.7° and 46.4°, respectively indexed as the (010) and (020) planes of a monoclinic $W_{18}O_{49}$ nanowires pattern (PDF 04-005-4314; cell constants: a = 18.32 Å, b = 3.79 Å, and c = 14.04 Å). The presence of only two peaks in the same diffraction axis can be correlated to an anisotropic growth of the crystallites alongside the longitudinal axis of the nanowire. Given the preferential growth of nanorods at the surface of the MoWOx particles and diffractograms obtained for these samples, it seems that these outer nanorods are mainly responsible for the crystallinity in the mixed formulations. Besides, the two $WO_{3-\delta}$ compounds can be indexed as a hexagonal WO_3 diffraction pattern (PDF 04-007-2322), with the difference that $WO_{3-\delta}$ 1h only exhibits part of the diffraction peaks, with weak and broad diffraction signals visible at 23.0°, 28.2°, 36.7°, 50.0° and 55.7° corresponding to the (001), (200), (201), (220) and (202) planes, respectively. The low crystallinity presented by this sample is probably due to the nanometric dimensions of the particles (limiting the crystallite size range that can be reached during the growth of the particles, measured at 30 nm by using Scherrer equation), while the larger $WO_{3-\delta}$ 12h hexagonal platelets can further crystallize during the longer solvothermal treatment they undergo (with an average crystallite size of 49 nm).

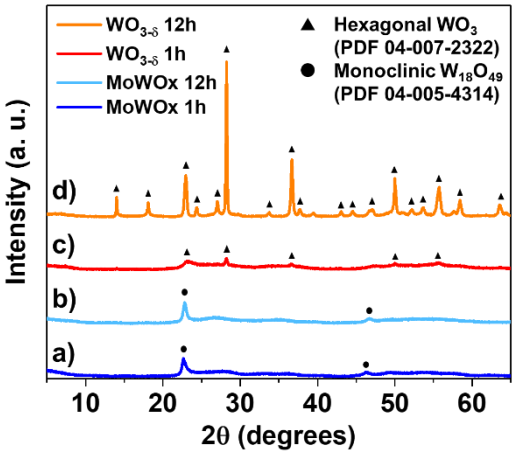

Figure 2: XRD diffractograms of (a) MoWOx 1h, (b) MoWOx 12h, (c) $WO_{3-\delta}$ 1h, and (d) $WO_{3-\delta}$ 12h powders. The diffraction scans are stacked at regular intervals of 100 counts.

2.1.3. Optical and electronic analyses of "MoWOx" 2/1 and $WO_{3-\delta}$ powders

The KM optical characterization of the powders diluted in LiF (10 wt. %, **Figure 3**) shows a strong increase in the absorption of the Mo-W mixed oxides formulations in comparison to parent $WO_{3-\delta}$ ones, as expected from previous studies,[8,47] but also a more intense absorption signal in both $WO_{3-\delta}$ 1h and MoWOx 1h than for their 12h counterparts. Furthermore, the absorption signature of MoWOx samples could be interpreted as a superposition of polaronic and plasmonic absorption signals, as previously reported in the literature.[6,46,53] Based on the deconvolution of the signals (see **Figure S4**), the optical signature of MoWOx 1h consists of two contributions, with a first peak centered at 750 nm (corresponding to the polaronic behavior), and a second one at 1350 nm (related to the plasmonic absorption). Moreover, MoWOx 12h exhibits peaks at 820 nm and 1900 nm, with the strong red-shift of the plasmonic signal being potentially due to the larger dimensions of the particles and to a reduction of the electronic density in the conduction bands, on which the LSPR frequency depends.[1,3,54,55] This shift towards higher wavelengths results in a large decrease and a broadening of the signal for the MoWOx 12h, stretching over a larger region of the spectrum, in comparison to the better defined peak observed for MoWOx 1h. For the $WO_{3-\delta}$ parent oxides, the signal is interpreted as a single contribution at 1470 nm in the 1h case: it is believed to correspond to a plasmonic resonance from selected literature[6,46,53] while being also consistent with a polaronic signature of thin films,[56] reminiscent of the lack of consensus on the dual band charge/discharge model (as discussed in the introduction). Meanwhile, no apparent peak is observed for $WO_{3-\delta}$ 12h.

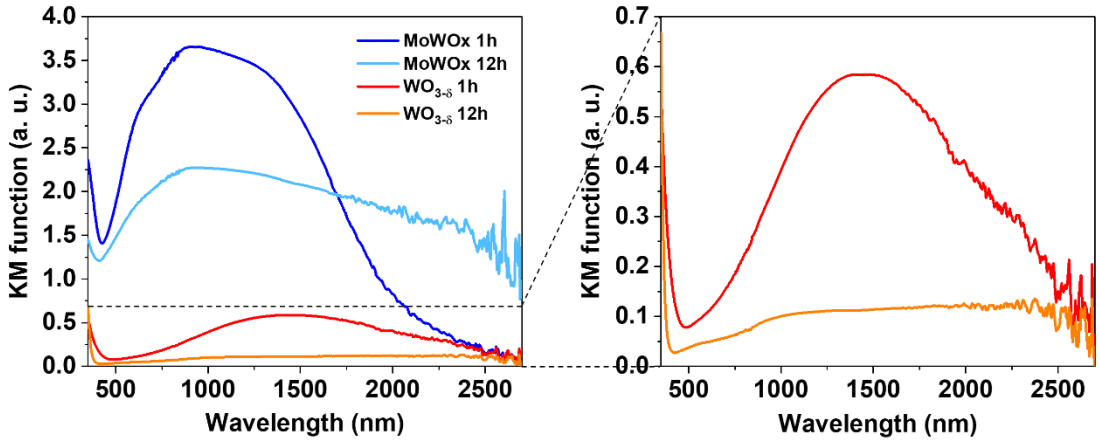

Figure 3: KM function obtained from diffuse reflectance data of the MoWOx 1h, MoWOx 12h, $WO_{3-\delta}$ 1h, and $WO_{3-\delta}$ 12h powders (all being diluted in a 90/10 LiF/sample ratio).

Given the optical results in Figure 3, an increased number of oxygen vacancies and reduced species is likely formed in the mixed formulations, and this specifically at the beginning of the solvothermal treatment (with greater absorption signals in the 1h samples compared to the 12h ones). This may owe to the nature of the isopropanol solvent (being proton donor and reducing agent[57,58]), potentially leading to the insertion of H^+ in the crystal lattice, and therefore of associated electrons (either free or localized over W^{5+} and Mo^{5+} species) to retain the charge neutrality. In addition, the substitution of Mo in the WO_3 octahedral sites of the MoWOx (and *vice versa* of W in the MoO_3 sites) could induce the formation of strains and defects, consecutively modifying the electronic and optical properties by creating color center (or polaronic) states and changing the band gap of the material.[8,59,60] As a consequence, the synergistic formation of both reduced species and free electrons originating from the creation of oxygen vacancies can lead to a significant boost in the optical properties of the MoWOx formulations in comparison to the parent oxides. In a second step, the particles could be partially re-oxidized during the remainder of the reaction time, due to their prolonged contact with the H_2O_2 reagent present in the synthetic media; this could result in having the 1h samples exhibiting a greater absorption signal than their 12h counterparts.

In order to confirm the preliminary assumptions on free electron density made from these optical results, XPS analysis is performed, first to evaluate the composition and oxidation states at the surface of the different compounds (**Figure 4** and **Table S1**). As for MoWOx samples, regarding molybdenum, both oxidized Mo^{6+} and reduced Mo^{5+} species are identified in MoWOx 1h and 12h as doublet contributions on Mo3d signals, respectively at 233.6 / 236.8 eV and 232.4 / 235.5 eV; for tungsten, only W^{6+} (and thus no W^{5+}) appears upon fitting of the W4f signals (doublet at 36.4 / 38.5 eV), highlighting the preferential trapping of the electrons over the molybdenum metallic centers at the surface of the particles.[14,43,61] The significant presence of reduced species is concomitant with the formation of oxygen defects in the crystal lattice, with some of the excess in electrons left from the missing oxygen trapped by metal atoms.[8,12,61,62] In addition, and even though this interpretation might be subject to much debate in the XPS field,[63] the presence of oxygen vacancies (O_{vac}) could be supposed from the O1s signal with a contribution at 532.6 eV, which also appears to be of the same intensity between both formulations. These results show very similar electronic surface properties in the mixed oxides regardless of the time under solvothermal treatment. However, since the XPS only probes the surface of the particles, the differences observed in the optical properties could arise from the bulk of the particles. As for the $WO_{3-\delta}$ parent oxide, a significant proportion of the W metallic centers are found to be in the W^{5+} state. Regarding O1s, the $WO_{3-\delta}$ 1h exhibits similar amounts of O_{vac}

to those found in the mixed oxide samples, while this contribution in the 12h formulation is found to be significantly less intense. In addition, the signal at 533.5 eV corresponds to weakly adsorbed C-O and O-H organic species. The increased contribution of the latter in $WO_{3-\delta}$ 12h (especially in view of the 532.1 eV signal) could indicate favorable crystalline faces at the surface of the hexagonal platelets, leading to a greater adsorption of organic impurities on the outer layer of the particles.

For semiconductor materials to support plasmonic features, such as the $WO_{3-\delta}$ materials investigated in this work, it is necessary that their concentration in free charge carriers increases beyond a threshold after which the material undergoes a transition to a degenerated semiconductor displaying a metallic behavior.[64–66] The four investigated formulations all support a large amount of reduced species and O_{vac}, leading to an oxygen substoichiometry that allows these WO_3-based materials to present LSPR properties.[54] That said, the lower concentration in reduced species and O_{vac} obtained for $WO_{3-\delta}$ 12h in comparison with the other formulations, as well as the large dimensions of the hexagonal particles (~2 µm), could limit their use as efficient plasmonic electrochromic materials.

Finally, Mo/W ratios are calculated, showing again that molybdenum-rich compositions are obtained for short-duration syntheses, with 3.7 and 1.6 Mo/W ratios determined for 1h and 12h, respectively, starting from a 2/1 ratio of Mo/W precursors in the reactive media. These results confirm that faster reaction kinetics occur for the Mo species, leading to a gradient going from the center of the urchins to the outer layer of surface nanorods. Noteworthy, Mo/W ratios calculated from XPS are smaller than EDX ones (see Figure S2), being of 4.7 and 2.0 for 1h and 12h by EDX, respectively. Since the XPS only probes the surface of the material, in comparison to the depth of analysis in the EDX measurements giving access to the bulk of the particles, XPS ratios are logically smaller than EDX ones, further confirming the concentric distribution of the Mo within the mixed oxide particles.

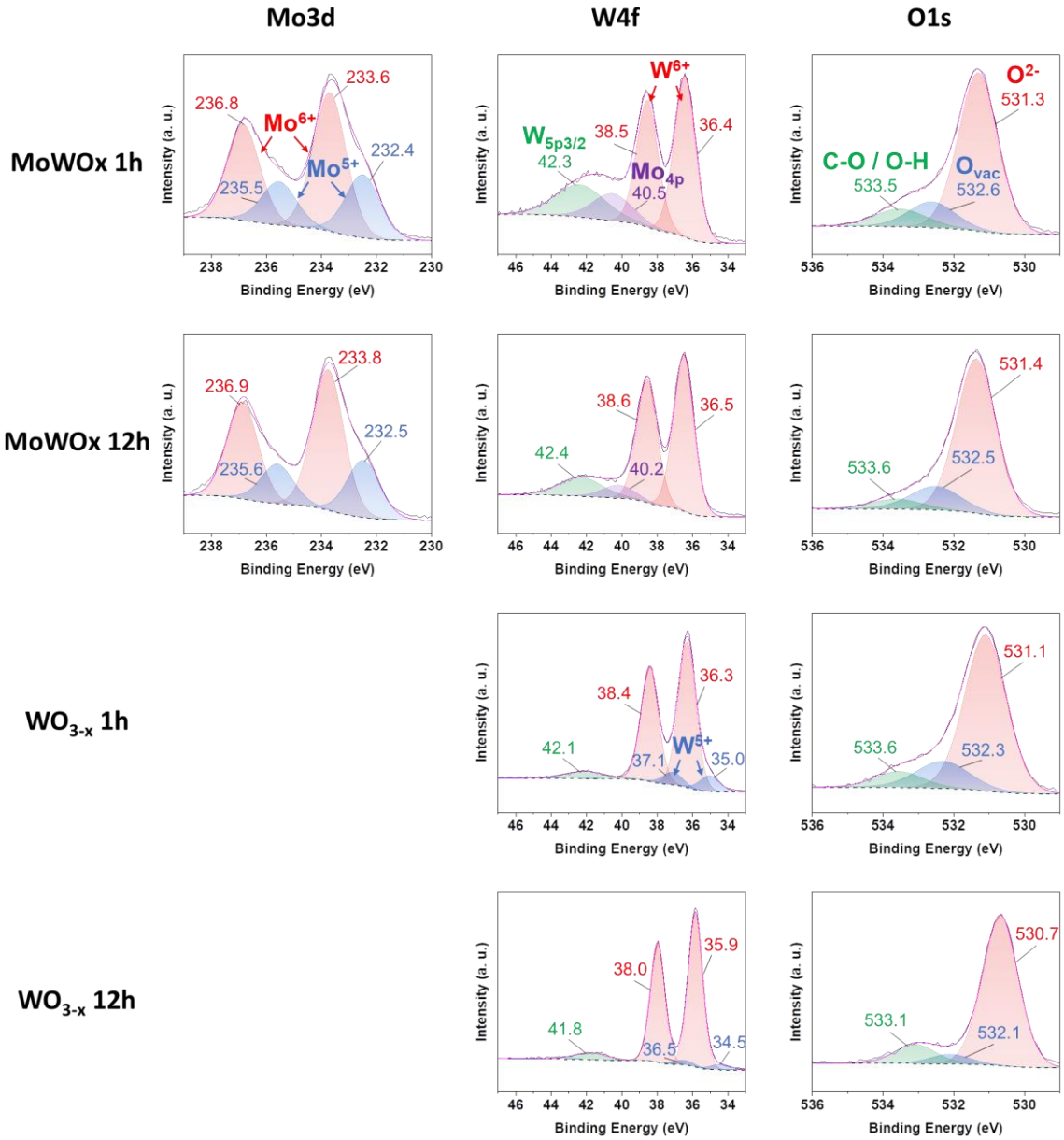

Figure 4: Mo3d, W4f and O1s XPS spectra of the MoWOx 1h, MoWOx 12h, $WO_{3-\delta}$ 1h, and $WO_{3-\delta}$ 12h powders.

EPR characterization is then carried out to assess the presence of free electrons, not only at the surface (as it is the case with XPS) but also in the bulk of the materials. This method allows the detection of unpaired electrons such as those trapped in the oxygen vacancies, those localized over reduced species such as W^{5+} ($5d^1$, $g \leq 1.9$) and Mo^{5+} ($4d^1$, $g \geq 1.9$) or those delocalized into the conduction band ($g < 2$). All four samples show large and well-defined signals below g-values of 2 (**Figure 5**), indicating that the electrons liberated by the formation of oxygen vacancies during the synthesis are either preferentially localized over metallic ions (yielding Mo^{5+} and W^{5+} reduced species), or delocalized into the conduction band to participate to the free charge carrier concentration. If the electrons were to be trapped inside the vacancies, the measured EPR response would rather appear as a very narrow signal, centered around a g-value close to 2.0023 corresponding to the free electron in vacuum (see the dashed line in Figure 5). The absolute concentration in all paramagnetic species, regardless of the proportion in the different elements (either reduced Mo or W, or free electrons in the conduction band), is proportional to the number of spins in the samples and to the area under the EPR absorption curves (**Figure S5** and **Table S2**) calculated by integration. Thus, the double integration of the EPR spectra follows a trend

regarding the concentration in reduced species and free electrons in the conduction band: MoWOx 1h > MoWOx 12h > $WO_{3-\delta}$ 1h > $WO_{3-\delta}$ 12h (cf. Figure S5), in good agreement with the ranking of optical absorption intensity (see Figure 3). In the bulk, MoWOx 12h has therefore 45% less reduced species and free conducting electrons than its 1h counterpart, while the signal of $WO_{3-\delta}$ 1h and 12h only represents 11% and 7% of that measured in the MoWOx 1h case.

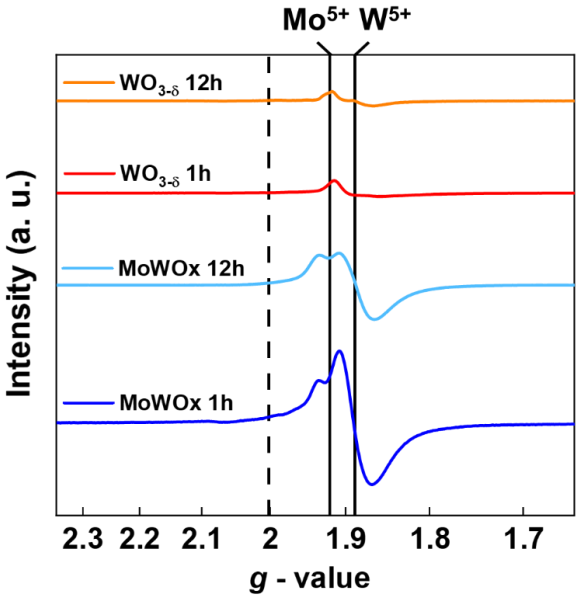

Figure 5: Low temperature X-band EPR spectra of the MoWOx 1h, MoWOx 12h, $WO_{3-\delta}$ 1h and $WO_{3-\delta}$ 12h powders.

All in all, there is a globally good match between XPS and EPR electronic measurements, and also with the UV-VIS-NIR optical results presented above. Consequently, the presence of a higher quantity in free charge carriers delocalized in the conduction band or localized on reduced species, whether at the surface or in the bulk of the materials, seems to translate into an increased absorption of the particles.

2.2. Spin-coated "MoWOx" and $WO_{3-\delta}$ films

2.2.1. Morphology and topography

MoWOx and $WO_{3-\delta}$ films are then deposited on glass substrates by spin coating (see details in Materials and Methods), and SEM top view micrographs of the samples are presented in **Figure S6**. Using a similar deposition protocol for all four cases, with equivalent quantities of each material being deposited at the surface of the substrate (same concentration and deposited volume across all suspensions), quite homogeneous films are obtained with thickness values of 1.16 ± 0.05 µm for MoWOx 12h, 0.21 ± 0.02 µm for $WO_{3-\delta}$ 12h, 0.84 ± 0.03 µm for MoWOx 1h and 0.87 ± 0.03 µm for $WO_{3-\delta}$ 1h (**Figure S7**). The strong decrease in thickness observed for the $WO_{3-\delta}$ 12h based films probably arises from a preferential orientation of the hexagonal $WO_{3-\delta}$ particles lying parallel to the surface of the substrate, and from a less homogeneous deposition process leading to non-covered regions of the substrate, visible in the micrograph. In the case of the $WO_{3-\delta}$ 1h formulation, the nanoparticles observed in the parent oxide rearrange themselves as microscale aggregates, leading to the deposition of a film with similar morphology and thickness to those of the 1h mixed oxide. Besides, films of MoWOx 12h are thicker in comparison with the other formulations, given the larger radius of the urchins obtained for this synthetic protocol.

2.2.2. Ex-situ electrochemistry

The active layers are then characterized by cyclic voltammetry (CV) in a 0.5 M $LiClO_4$ in propylene carbonate electrolyte solution. A characteristic curve is obtained for both $WO_{3-\delta}$ formulations (**Figure 6**), with a reduction wave starting around -0.1 V (vs. Ag/AgCl) and a return oxidation peak around -0.8 V. In the case of the MoWOx films, the general shape of the CV is retained while the anodic peak appears to comprise two overlapping signals, that could correspond to the oxidation of tungsten (into W^{6+}) around -0.8 V, and molybdenum (into Mo^{6+}) at -0.3 V. The capacity extracted from these electrochemical measurements, presented in **Table 1**, highlights at least a threefold increase in capacity in MoWOx layers in comparison with $WO_{3-\delta}$ ones, notably the two 1h samples being of similar thicknesses of 0.8-0.9 µm: 42.8 mC cm^{-2} for MoWOx, 13.5 mC cm^{-2} for $WO_{3-\delta}$. This large improvement in capacity probably arises from the presence in large amounts of molybdenum in the mixed formulations,[45] which theoretical capacity (MoO_3, 1117 $mAhg^{-1}$[67]) is superior to that of WO_3 (693 $mAhg^{-1}$[68]). Indeed, Elezzabi *et al.* have reported that while W can mostly be reduced from W^{6+} to W^{5+}, Mo can be reduced from Mo^{6+} to Mo^{5+} and then further reduced to Mo^{4+}, if the structural properties of the material allow it, resulting in the exchange of an additional electron and thus a higher specific capacity.[45] In addition to the redox properties of both oxides, the crystalline structure adopted by the material also comes into play, allowing more or less cationic insertion into the structure. Even though the presence of Mo^{4+} in our mixed oxides has not been highlighted in this work, notably in view of the XPS results, it is expected that the capacity of the mixed oxides would increase in comparison to the pure tungsten parent oxides, given that our MoWOx formulations consist mostly in molybdenum. Following a similar argument, the capacity of MoWOx 1h is greater than that of MoWOx 12h, 42.8 mC cm^{-2} vs. 28.9 mC cm^{-2}, as expected from the Mo-rich 1h compound (5/1 Mo/W ratio vs. 2/1 for the 12h sample). The presence of a large concentration in oxygen vacancies (responsible for the release of numerous unpaired electrons, leading to the intense EPR response of the mixed oxides) could also be the reason for the observed increase in capacity, possibly increasing the conductivity of the sample and acting as active sites for the redox reactions.[69,70]

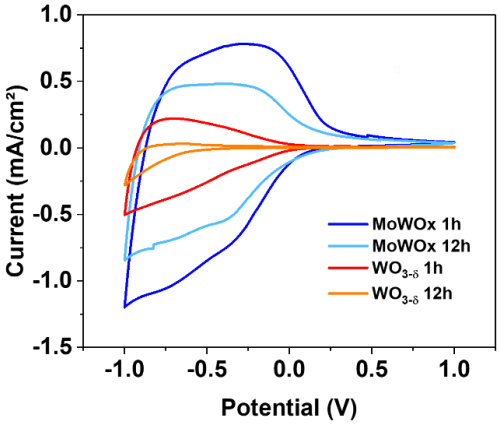

Figure 6: CV curves (5th cycle at 20 mV s^{-1}, measured in 0.5 M $LiClO_4$/PC vs. Ag-AgCl) of MoWOx 1h (blue), MoWOx 12h (cyan), $WO_{3-\delta}$ 1h (red) and $WO_{3-\delta}$ 12h films (orange).

Table 1: Capacity calculated from the CV curves of MoWOx 1h, MoWOx 12h, $WO_{3-\delta}$ 1h and $WO_{3-\delta}$ 12h films.

		Capacity [mC cm^{-2}]	Identified oxidation peaks
MoWOx	**1h**	42.8	-0.7 V, -0.4 V
MoWOx	**12h**	28.9	-0.7 V, -0,4V
WO_{3-X}	**1h**	13.5	-0.7 V
WO_{3-X}	**12h**	3.3	-0.6 V

2.2.3. In-situ spectroelectrochemistry

Contrasts and coloration efficiencies

Spectroelectrochemical characterization of the films is carried out in potentiostatic mode to study their dual-bald electrochromic functionality. Similarly to the electrochemical measurements above, 0.5 M $LiClO_4$ in propylene carbonate is used as electrolyte. Here, various potential values, progressively decreasing from +1.0 to -1.0 V vs. Ag-AgCl by -0.5 V steps, are applied for 5 minutes each before the acquisition of the transmittance spectra between 350 and 1650 nm, and this in order to reach a stable optical state. The quantified transmittance values are expressed as the averaged transmittance over a given range of wavelength (350 to 750 nm for the VIS region, and 750 to 1650 nm for the NIR range, see Materials and Methods). As shown in **Figure 7** and **Table 2**, both MoWOx formulations and $WO_{3-\delta}$ 1h display a dual-band behavior, as described above, evolving from a bleached state at +1.0 V to an intermediate state displaying LSPR-based NIR darkening abilities at progressively reduced potentials (+0.5 and +0.0 V). Then, as the voltage reaches more reducing values, the transmittance keeps lowering in the NIR and starts to decrease in the VIS region as well, allowing a third, fully-darkened optical state. Interestingly, no dual-band behavior is observed in the $WO_{3-\delta}$ 12h, certainly as the consequence of its (deduced) low quantity in free charge carriers, reduced species and oxygen vacancies (as shown from the combination of EPR and XPS results), as well as the micrometric dimension of the particles limiting their ability to support LSPR features.

According to previous electrochromic literature,[1,2,4,17,30] the behavior of dual-band materials, requiring different potential ranges to activate the desired modulation, relies on competitive polaronic *vs.* plasmonic mechanisms, which are based on faradaic *vs.* capacitive charge/discharge processes. The considered studies suggest first a plasmonic-based NIR-selective modulation that should be active at slightly reducing potentials, given its capacitive behavior, with the faradaic process then occurring once more reducing potentials are reached – which is required to promote the insertion of cations from the electrolyte into the active material.[1,2,4] Even though this approach is considered for the discussion of the results presented later in this work, other interpretations have been proposed (see *Introduction*), especially questioning the link between the capacitive/faradaic mechanisms and the plasmonic/polaronic activity they are respectively associated with.[4,17–20,22–24] In this case, the first model seems possible for the presently studied systems.

Photographs illustrating the appearance of films produced from all four formulations as a function of the applied potential are further presented as insets in Figure 7, and their L*a*b* parameters are included in **Table S3**. Very interestingly, the electrochromic properties exhibited by the MoWOx formulations, especially the 1h case, appear to deviate from the usual dual-band behavior reported in the literature for $WO_{3-\delta}$ based materials[4,14–17] and recalled in the previous paragraph. Indeed, in their

most oxidized state (at +1.0 V), MoWOx 1h and 12h display some absorption in the VIS range (46.8% and 58.1% of averaged transmittance) together with relatively high transparency in the NIR (averaged transmittance of 76.1% and 70.5%, respectively). This optical absorption response arises from the strong, enhanced absorption signal provoked by the Mo-W mixing (see Figure 3), that in turn lowers the maximal transmittance values that can be reached in the wavelength range around its maximum optical response (here 850-900 nm, corresponding to the superposition of the polaronic and plasmonic signals observed in the optical characterization of the powders). Instead of going from a VIS-bright state to first an intermediate cool state (VIS-bleached, NIR-darkened) and then a fully VIS- and NIR-darkened state, the MoWOx samples start from a "warm" transmission mode (NIR-transparent and VIS-darkened), then undergoes NIR opacification before finally achieving the fully VIS- and NIR-darkened state. To the best of our knowledge, such "warm" mode[29–31] and consecutive NIR then VIS modulation has not been reported yet for Mo- or W-based electrochromic formulations.

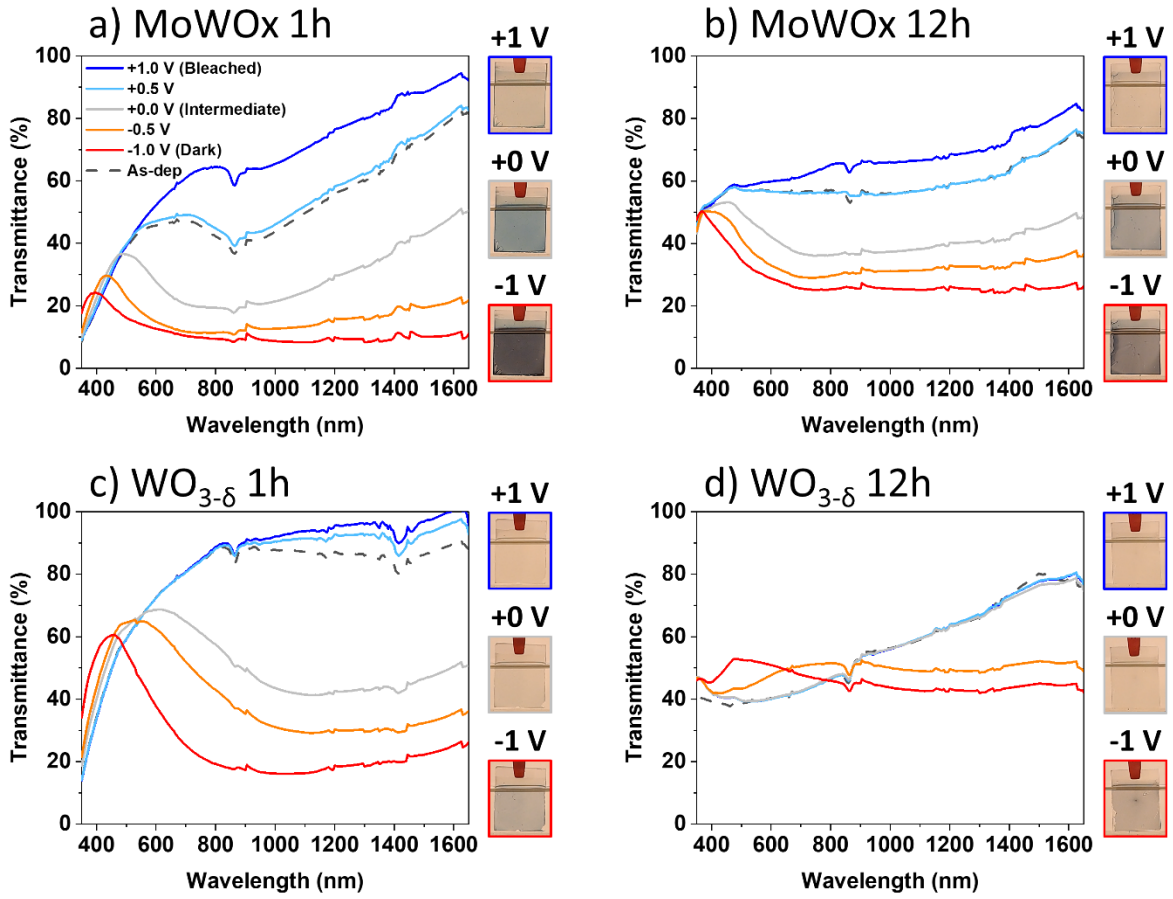

Figure 7: SEC transmittance spectra of (a) MoWOx 1h, (b) MoWOx 12h, (c) $WO_{3-\delta}$ 1h and (d) $WO_{3-\delta}$ 12h films biased in the $LiClO_4$-PC electrolyte, as a function of the applied potential. Pictures of the films in the bleached (+1 V), intermediate (+0 V) and dark state (-1 V) are shown as insets next to the corresponding spectra.

Table 2: Summary of the SEC data in $LiClO_4$-PC.

	Bleached (+1.0 V)		Intermediate (+0.0 V)							Dark (-1.0 V)						
	T [%]		T [%]		ΔT [%]		Q_{in} [mC cm^{-2}]	CE [cm^2 C^{-1}]		T [%]		ΔT [%]		Q_{in} [mC cm^{-2}]	CE [cm^2 C^{-1}]	
	VIS	*NIR*	VIS	*NIR*	VIS	*NIR*		VIS	*NIR*	VIS	*NIR*	VIS	*NIR*		VIS	*NIR*
MoWOx 1h	46.8	*76.1*	31.1	*30.8*	15.8	*45.3*	-11.2	15.9	*35.1*	23.3	*9.5*	23.5	*66.6*	-82.1	3.7	*11.0*
MoWOx 12h	58.1	*70.5*	45.0	*40.5*	13.0	*30.0*	-9.6	11.5	*25.1*	34.0	*25.5*	24.0	*45.0*	-59.0	3.9	*7.5*
$WO_{3-\delta}$ 1h	61.3	*93.8*	58.7	*46.3*	2.6	*47.5*	-3.0	6.3	*102.2*	42.6	*19.4*	18.7	*74.5*	-32.7	4.8	*21.0*

In the case of MoWOx 1h, contrasts of 15.8% and 45.3% are obtained for the intermediate state, in the VIS and NIR regions respectively, while the colored state exhibits a modulation of 23.5% and 66.6% in those same ranges. The CE of the material reaches values of 15.9 $cm^2 C^{-1}$ (VIS) and 35.1 $cm^2 C^{-1}$ (NIR) in the intermediate state, and 3.7 $cm^2 C^{-1}$ and 11.0 cm^2C^{-1} in the darkened state. The MoWOx 12h displays a modulation of 13.0% in the VIS and 30.0% in the NIR at +0.0 V, then these values respectively go up to 24.0% and 45.0% once -1.0 V is applied. This formulation displays CE of 11.5 $cm^2 C^{-1}$ and 25.1 $cm^2 C^{-1}$ in the NIR-preferential state, and 3.9 $cm^2 C^{-1}$ and 7.5 $cm^2 C^{-1}$ in the most reduced state, for VIS and NIR regions respectively. For the third dual-band formulation, $WO_{3-\delta}$ 1h, contrasts in the VIS and NIR ranges respectively reach 2.6% and 47.5% in the intermediate state, and 18.7% and 74.5% in the darkened state. In the latter case, the material exhibits CE values of 6.3 $cm^2 C^{-1}$ and 102.2 $cm^2 C^{-1}$ at +0.0 V and 4.8 and 21.0 $cm^2 C^{-1}$ at -1.0 V. For all three active formulations, the additional ability to further oxidize the "as-deposited" state by applying a +1.0 V potential is in good agreement with the assumption that the formation of reduced species, especially with MoWOx configurations, could be due (at least partially) to the insertion of protons provided by the isopropanol in the reactive media into the crystal lattice during the solvothermal process,[8] which can in turn be extracted from the material during the electrochemical cycling. The fourth case, $WO_{3-\delta}$ 12h, has not been evaluated in terms of figures of merit in view of its poor intrinsic EC behavior.

Noticeably, in the three considered formulations, the CE of the intermediate state is clearly superior to that of the darkened state: indeed, almost half of the total optical change (especially in the NIR) is already reached at +0.0 V for only 10-16% of the total charge inserted in the darkened mode. As stated earlier, such high efficiency can be linked to a capacitive behavior. These results, in addition to the optical and electronic characterizations of the precursor powders presented earlier, attest the ability of the two MoWOx formulations, as well as the $WO_{3-\delta}$ 1h, to support a dual-band behavior being potentially LSPR-based. From the contrast and CE values presented in Table 2, MoWOx 1h shows better performances than its 12h counterpart, especially in the NIR region. This improved behavior at shorter solvothermal treatment could result from the differences observed in the powders, with smaller particle size and increased free charge carrier concentration (as shown in the EPR spectra, Figure 5), leading to a higher surface area and an enhanced optical absorption (see Figure 3).

Kinetics

In addition to its contrasts and CEs, the performance of an electrochromic material also depends on its ability to switch between optical states in an adequate time frame. Presently, the kinetics of the films are measured at three wavelengths, 550, 1000 and 1550 nm, over 10 minutes for each potential step. So-called coloration/bleaching times (t_c and t_b, respectively) correspond to the duration required to reach 90% of the contrast between the bleached and colored state (or reversibly). The coloration

and bleaching kinetics of the two MoWOx and the $WO_{3-\delta}$ 1h samples are summarized in **Figure 8** and **Table 3**.

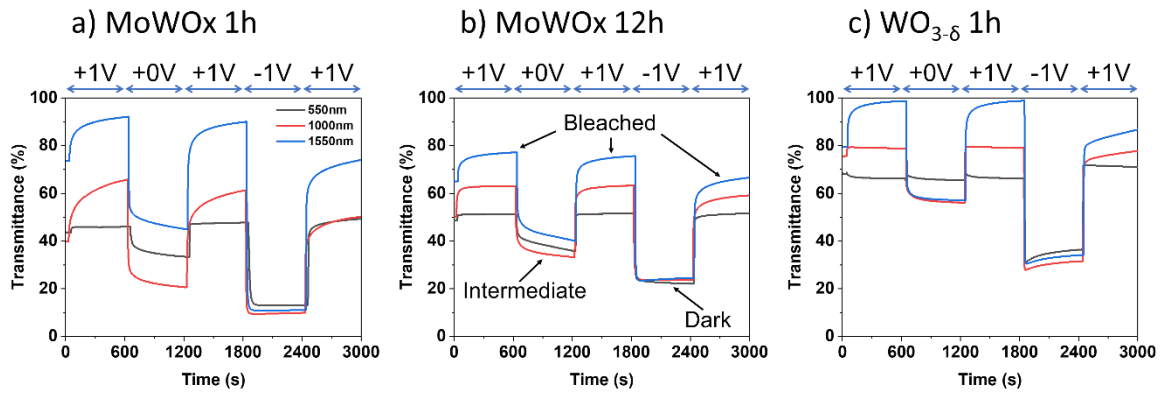

Figure 8: SEC transmittance curves of the films obtained from the three dual-band formulations (a) MoWOx 1h, (b) MoWOx 12h, (c) $WO_{3-\delta}$ 1h, as a function of time and applied potential, for three distinct wavelengths (black curve: 550 nm, red curve: 1000 nm, blue curve: 1550 nm).

Table 3: Summary of the SEC kinetics data obtained on MoWOx 1h, MoWOx 12h and $WO_{3-\delta}$ 1h films.

	Intermediate (+0.0 V)						**Dark (-1.0 V)**					
	t_c [s]			**t_b [s]**			**t_c [s]**			**t_b [s]**		
	550 nm	1000 nm	1550 nm	550 nm	1000 nm	1550 nm	550 nm	1000 nm	1550 nm	550 nm	1000 nm	1550 nm
MoWOx 1h	304	74	110	6	252	140	28	8	10	58	160	114
MoWOx 12h	410	138	198	6	52	80	16	16	10	14	106	104
$WO_{3-\delta}$ 1h	484	88	22	2	4	72	6	4	6	4	24	68

To begin with, for all three formulations, the coloration time in the VIS region at the intermediate bias (+0.0 V) appears very long for a very limited modulation (around 10% at best), reaching values ranging from 300 to 500 seconds. Besides, the NIR modulation takes place at faster rates, with a maximum in t_c of 198 s, while displaying greater contrasts (close to 40%). These results highlight the NIR-selective modulation (mainly plasmonic) exhibiting faster kinetics than the VIS modulation (mainly polaronic). During the reverse bleaching step, the discoloration in both VIS and NIR regions is carried out at significantly faster paces, with the exception of MoWOx 1h in the NIR range, exhibiting the longest bleaching times recorded across the three investigated formulations. Regarding the dark state (-1.0 V), the coloration appears very quick since the greater difference in potential allows the easier insertion of the Li^+ cations from the electrolyte into the active layer, resulting in fast kinetics even for large contrasts (30-40% and 60-80% in the VIS and NIR regions, respectively). The discoloration of the darkened state is faster in the VIS region, while the bleaching in the NIR presents slower kinetics, probably due to charge trapping inside the particles, leading to residual darkening after the electrochemical cycling.

Globally, these results highlight the ascendancy of the capacitive mechanisms at moderate bias, which is then caught up by the faradic behavior once a more reducing potential is applied. However, in comparison with other plasmonic materials of the literature,[4,17] quite long switching times are noticed for the NIR modulation, especially for both MoWOx 1h and 12h in comparison to $WO_{3-\delta}$ 1h. On the

basis of the results presented here, these slow kinetics could be due to the complexity of the urchin-like MoWOx particles that somehow hinders the available surface area and increases the mean free path of the positive counter-ions (here Li^+ cations) that have diffused from the bulk electrolyte to the active material surface. In the case of MoWOx 1h, the smaller dimensions of the particles translate into an even more compact packing of the nanorods around the core, further impeding the diffusion of the cations towards the active surface. In comparison, the nanospherical morphology of the $WO_{3-\delta}$ 1h offers larger surface area and shorter diffusion paths, thus globally improving the commutation kinetics for this material.

Capacitive vs. faradic mechanisms

In order to further analyze the capacitive behaviors expected from the materials, the spin coated films are electrochemically biased in a 0.5 M $TBAClO_4$ – PC electrolyte. Given the very large radius of the TBA^+ cations, ionic insertion into the crystal lattice of the active layers is prohibited. Therefore, any measured optical change has to originate from a capacitive charge/discharge of the materials. This limitation in the available electrochemical processes is clearly visible in the transmittance spectra and data presented in **Figure S8** and **Table S4**, with the darkening taking place preferentially in the NIR and reaching optical states similar to the +0.0 V intermediate state obtained with the lithiated electrolyte. Indeed, the MoWOx 1h reaches contrasts of 10.4% (VIS) and 32.9% (NIR) in the intermediate state (+0.0 V), going up to 12.3% (VIS) and 44.3% (NIR) when applying -1.0 V. In the 12h mixed oxide, the VIS contrast ranges from 8.0% at +0.0 V and 8.1% at -1.0 V, while the NIR modulation in the intermediate mode comes up to 23.6% and 24.4% in the colored state. Besides, the 1h parent oxide displays contrasts of 0.5% (VIS) and 22.2% (NIR) in the intermediate +0.0 V state, and -0.4% (VIS) and 26.3% (NIR) in the darkened state. Finally, in the case of $WO_{3-\delta}$ 12h, no modulation appears upon cycling in $TBAClO_4$, indicating the lack of sufficient optoelectronic features in order to display the sought dual-band behavior. Pictures of the films are included as insets in Figure S8 while the L*a*b* parameters of the films are summarized in **Table S5**. In all three dual-band active formulations, the modulation in $TBAClO_4$ almost reaches completion at +0.0 V, with a few extra percent of contrast gained when a bias of -1.0 V is achieved, recreating an optical state very similar to the intermediate state (+0.0 V) that was obtained in the lithiated electrolyte. These performances are in good accordance with what was expected from this experiment, limiting the modulation to the capacitive mechanisms, predominantly present in the intermediate state according to the model used for the interpretation of this work.

From the results respectively obtained in $LiClO_4$ and $TBAClO_4$, it is possible to estimate the proportion of capacitive-related modulation in the materials (cf. Materials and Methods for calculation details, and **Table S6**). These estimations show a greater percentage of the latter in the MoWOx formulations in comparison to the $WO_{3-\delta}$ 1h: the capacitive mechanisms represent 69.2% and 70.1% of the intermediate state, and 59.4% and 44.0% of the darkened state of the MoWOx 1h and 12h, respectively, while the 1h parent oxide only exhibits 32.9% at +0.0 V and 18.7% at -1.0 V. These values are in good accordance with the optical and EPR characterizations of the powders presented above, which indicated a larger quantity of unpaired electrons in the MoWOx formulations in comparison to the pure oxides, with a significant proportion being delocalized in the conduction band and leading to a greater contribution of the capacitive behavior in the electrochromic performances of the materials. In addition, the decrease in capacitive contribution at -1.0 V, observed in all formulations, was anticipated since the electrochemical mechanisms in this second working regime are a combination of capacitive behavior and faradaic charge/discharge in the lithiated electrolyte (while the $TBAClO_4$-PC electrolyte is limited to capacitive mechanisms). The same calculation can then be carried out for the inserted charges: since both the optical change and the quantity of inserted charges are important for

the electrochromic performances of a material, the capacitive proportion of optical modulation can be divided by that of inserted charges in order to obtain a figure of merit equivalent to the CE, but for the contribution of the capacitive behavior (*K*) in the different formulations (cf. *Materials and Methods*). Higher values are consecutively determined for the mixed oxides in comparison to the parent oxide, with MoWOx 1h displaying the greatest capacitive contribution out of the three dual-band formulations (1.46 and 1.79 in intermediate and darkened modes, respectively, vs. 1.12 and 1.30 for MoWOx 12h, and 0.82 and 0.45 for $WO_{3-\delta}$ 1h), once again highlighting the potential of this material for future developments.

Reversibility

Finally, the evaluation of the reversibility of the optical changes undergone by the different materials is performed. Transmittance modulation spectra of MoWOx 1h and 12h, and of $WO_{3-\delta}$ 1h and 12h samples are presented in **Figure 9**, being biased between +1.0 and -1.0 V for 5 cycles, with pictures of the first and fifth cycles. In addition, the evolution of the L*a*b* parameters of the films during the electrochemical cycling are shown in **Table S7**. In MoWOx 1h, a significant drop of transmittance in the bleached state already appears after the second cycle (minus 20 % in the NIR, stable in VIS), followed by a stabilization of the transmittance values in both bleached (+1.0 V; 43.6% and 51.6% in VIS and NIR, respectively) and darkened states (-1.0 V; 15.5% in VIS and 27.5% in NIR). The loss of transmittance appearing after the first coloration seems to indicate some propensity to irreversible Li^+ insertion in some of the active sites. On the other hand, MoWOx 12h and $WO_{3-\delta}$ 1h display a similar stability of the colored state (maximum of 5-6% change in MoWOx 12h and 10-11% in $WO_{3-\delta}$ 1h, versus 4-6% in MoWOx 1h) but a more gradual decay of the bleached state (minus 7.1% and 4.4% after the first coloration in MoWOx 12h and $WO_{3-\delta}$ 1h, respectively). Nevertheless, in all 3 cases, an optical state similar to the "as-deposited" state is obtained within the first two cycles. One possible explanation of this process could be that the H^+ potentially present in the "as-deposited" samples (originating from the reducing effect/proton-donor effect of the isopropanol in the reactive medium) can be electrochemically extracted from the materials, with the transmittance of the film increasing to reach the +1.0 V state. However, after the first coloration, due to their size difference, Li^+ could be irreversibly inserted in the sites previously occupied by the protons, irremediably modifying the crystalline properties of the material, as previously reported for other metal oxides (such as $Li_{1.12}(Ni_{0.425}Mn_{0.425}Co_{0.15})_{0.88}O_2$,[71] $Li_xH_{1-x}NbO_3$,[72] $H_2Ti_6O_{13}$,[73] MnO_2[74]) and thus limiting the transmittance of the films to their previous "as-deposited" state. Finally, in the case of the $WO_{3-\delta}$ 12h, the bright and dark states almost completely merge after the first coloration cycle, thus not fulfilling the requirements to be considered as an electrochromic material, which should exhibit a reversible modulation of its optical properties upon the application of a potential.

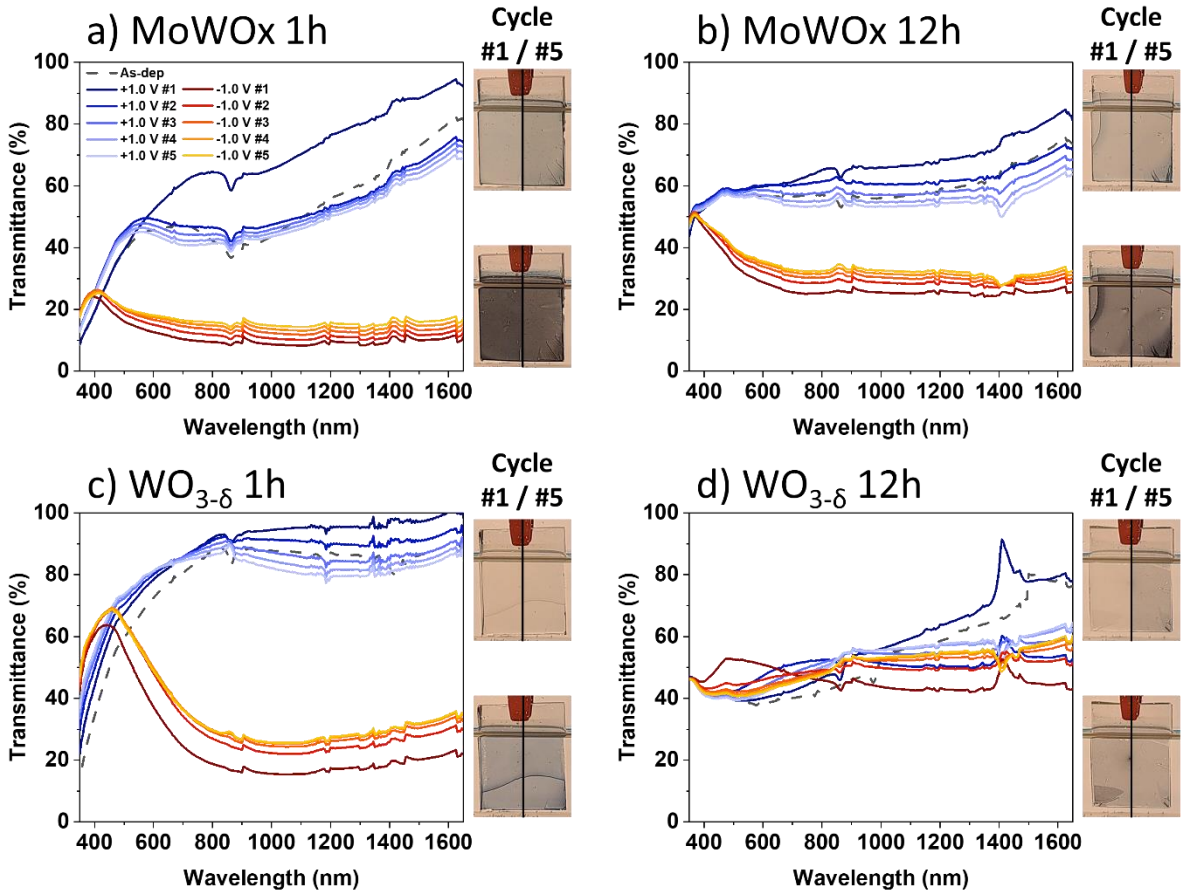

Figure 9: SEC transmittance spectra of (a) MoWOx 1h, (b) MoWOx 12h, (c) $WO_{3-\delta}$ 1h and (d) $WO_{3-\delta}$ 12h films biased in the $LiClO_4$-PC electrolyte, as a function of the electrochemical cycling.

All in all, the results obtained from the characterizations of the films highlight the remarkable properties of $WO_{3-\delta}$ 1h and both MoWOx, especially MoWOx 1h, as dual-band plasmonic electrochromic materials. In all active formulations, it was possible to demonstrate the preferential modulation of NIR wavelengths at slightly reducing potentials; the origin of this NIR-selective activity seems to arise from a capacitive/plasmonic behavior as proposed from the SEC measurements in $TBAClO_4$-PC. Amongst the mixed oxides, MoWOx 1h exhibits the most promising performances, owing to a greater quantity of free charge carriers leading to a greater optical absorption. Even though $WO_{3-\delta}$ 1h displays faster kinetics and a more selective modulation towards NIR in the intermediate state (+0.0 V), a greater proportion in capacitive behavior is shown in both MoWOx formulations. In addition, the MoWOx formulations, especially in the 1h case, display a very peculiar and novel optical behavior in the as-deposited state and after +1.0 V polarization ("bleached"), involving a large transmittance in NIR coupled with relatively strong absorption in VIS corresponding to a so-called "warm" optical mode (VIS/light-blocking and NIR/heat-transparent).

3. Conclusions and perspectives

Novel electrochromic materials based on mixed molybdenum – tungsten oxide formulations ($Mo_yW_{1-y}O_{3-\delta}$, "MoWOx") have been obtained from a single-step solvothermal synthesis procedure, with various Mo/W stoichiometries and reaction times being investigated. These compounds have been further spin-coated into thin films that attest dual-band optical modulation. Specifically, a VIS/NIR-selective electrochromic behavior is observed in MoWOx 2/1 formulations obtained after 1h and 12h of synthetic duration, as well as in the parent $WO_{3-\delta}$ formulation obtained after 1h; a preferential NIR-darkening is obtained when a slightly reducing potential of +0.0 V (vs. Ag/AgCl) is applied, followed by an opacification over both VIS and NIR regions when using a more reducing potential of -1.0 V. The dual-band properties exhibited by these materials are correlated to the presence of a large amount of unpaired electrons, obtained through the promoted formation of oxygen vacancies and reduced species during the synthesis, and to the presence of nanostructures (nanospheres of $WO_{3-\delta}$ 1h, and nanorods at the surface of the MoWOx urchins) allowing them to support LSPR features. Amongst the mixed oxides formulations, MoWOx 1h displays the most remarkable optical performances, with large transmittance contrasts in both VIS (23.5 %) and NIR (66.6 %) regions, as well as a greater proportion in the capacitive contribution to the electrochromic processes. Nevertheless, the parent $WO_{3-\delta}$ 1h formulation exhibits higher coloration efficiencies than both MoWOx oxides, mostly because of the nanospherical morphology of the particles probably providing more surface area for the plasmonic features to be expressed. In addition, while the presently processed $WO_{3-\delta}$ nanostructures display a behavior similar to what was expected from previous work of the literature,[4,14–17] MoWOx compounds testify for the occurrence of a "warm" mode (VIS-darkened, NIR-transparent) in the as-deposited state and after +1.0 V polarization ("bleached"), which, to the best of our knowledge, has not been reported so far with tungsten or molybdenum oxide based electrochromic materials. This uncommon optical state is therefore uniquely obtained thanks to the large quantity of free charge carriers originating from the Mo/W mixing process, leading to a strong optical absorption signal centered around 850-900 nm.

Within the scope of this research work, the dual-band electrochromism of MoWOx has been attributed to the presence of both plasmonic excitation (in NIR) and polaronic-like resonance (in VIS), in line with the proposed interpretation of the electrochemical response of reported $WO_{3-\delta}$ nanoparticles[1,2,4] and with the detailed analysis of the Kubelka-Munk experiment on the compounds studied herein.[48] The debate of the link between the doping mechanism (capacitive/faradaic) and the type of excitation (plasmonic/polaronic) is however still open. The clear modification of the optical response when the redox potential reaches negative-enough values to allow the cation insertion supports the hypothesis of a causal relation between the cationic insertion and the polaronic optical response. However, modelling works in literature have shown that inserted cations are totally ionized and occupy existing cavities in WO_3 with no local deformation of the atomic structure.[19,75] In that case, both capacitive and faradaic doping would have the exact same effect on the optical response. The modification of the structural parameter following the cation insertion could then be associated with the charge doping of the crystal.[23] Further experimental and numerical investigations are required to settle the debate, but this goes beyond the scope of the present work.

Future developments of MoWOx materials processing should be directed towards the consolidation of their electrochromic performances, notably the switching speed and reversibility. Moreover, additional electrochemical characterization will be required to better understand the limitations faced by the MoWOx materials. For example, by modifying the shape and size of the counter electrode to avoid high current densities that could damage the sample, or by monitoring the ageing of the samples during cycling at given temperature and humidity levels. If necessary, the synthetic and deposition

processes could be adapted in order to obtain more favorable morphologies, optical and electronic properties, leading to improved performances of the films. The addition of surfactant or different solvents (or mix of aqueous/organic solvents) to the solvothermal process could be investigated in an attempt to favor the production of nanometric particles, more inclined to display highly efficient plasmonic optical properties. In addition, several other synthetic paths could be explored, such as colloidal synthesis or supercritical processes, but also different deposition methods like spray coating,[76] allowing for the scale-up of the film processing. Finally, the next step after reaching convincing electrochromic properties will be to fabricate full devices comprising the active layer, a suitable counter electrode material (either electrochromically active such as NiO, or optically neutral/passive such as CeO_2), and an electrolyte layer, all incorporated between two conducting glass substrates.

With this work as a first demonstration of the original, advanced optical functionality of the MoWOx formulations, the results presented herein are very promising for the future development of highly efficient, dual-band electrochromic systems based on these mixed oxides formulations. Relying on the enhanced efficiency and selectivity of these materials towards VIS and NIR wavelength ranges, looking into their ability to access multiple working modes, including the warm state, the MoWOx formulations are promising candidates for the development of “new generation” dual-band smart windows. Such a remarkable solar filtration behavior could ultimately be of great interest to improve the functionality of fenestration solutions in buildings by broadening the modes of solar tunability, and therefore the adaptability range of the devices towards different weathers, seasons, geographies and/or user needs.

4. Materials and Methods

Materials: Metallic tungsten (W, fine powder, 99+%) and molybdenum powders (Mo, 99+%) are purchased from Merck, isopropanol (technical) and hydrogen peroxide (H_2O_2, 33%) from VWR, lithium fluoride (LiF, 99.8% anhydrous) is supplied from ROC/RIC, lithium perchlorate ($LiClO_4$, 95% anhydrous) by Alfa Aesar, tetrabutylammonium perchlorate ($TBAClO_4$, 99+%) and propylene carbonate (PC, 99.7% anhydrous) from Sigma-Aldrich. 50 x 50 cm Planibel G fast (15 Ω/square) glass panels are graciously supplied by AGC Glass Europe and manually cut into 2.0 x 2.5 x 0.4 cm conducting transparent substrates. All reagents are used as received without further purification.

Synthesis of $Mo_yW_{1-y}O_{3-\delta}$ and $WO_{3-\delta}$ compounds: In a typical solvothermal synthetic procedure,[8] H_2O_2 (11.5 mL) is added to tungsten metallic powder (3 mmol) and molybdenum metallic powder (6 mmol) (Mo/W molar ratio = 2/1) and magnetically stirred for 1h, yielding a clear yellowish solution. This solution is mixed with isopropanol (69 mL) into a Teflon vessel (125 mL), which is then sealed in a stainless-steel autoclave, heated and maintained at 160°C for a duration varying from 1 to 12h. Following the cooling of the solvothermal reactor down to room temperature, the obtained suspension is collected, centrifuged and rinsed with ethanol three times, and finally dried under vacuum at 60°C overnight. The protocol is repeated with adapted Mo/W ratio for the synthesis of the 1/1 (4.5 mmol of tungsten and molybdenum) and 1/2 formulations (6 mmol of tungsten and 3 mmol of molybdenum). For the $WO_{3-\delta}$ parent oxide, the same protocol is applied without the addition of molybdenum powder (thus with 9 mmol of tungsten).

Film deposition: Suspensions of each formulations are spin coated onto conducting glass substrates, previously cleaned by sonication in acetone and ethanol, further dried under compressed air stream and finally treated by UV-O_3 for 20 minutes. A suspension in ethanol (50 µL, 125 mg/mL) is dynamically deposited onto the substrates, being rotated at 2000 rpm for 1 minute. The samples are subsequently dried for 5 minutes at 100°C on a hot plate, and further submitted to a "flash" heating treatment of 1 minute at 250°C on a hot plate.

Characterizations: Micrographs of the particles are obtained from transmission electron microscopy (TEM) using a TECNAI G^2 20 operated at 200 kV. Top-view images of the spin coated films are acquired on a scanning electron microscope (SEM) TESCAN CLARA equipped with an energy dispersive X-ray spectroscopy (EDX) detector, so to determine particles dimensions (excepted for the $WO_{3-\delta}$ 1h, measured on the TEM micrographs) and molar ratios of the mixed oxides. Films thickness is measured by a Dektak stylus profilometer. X-ray diffraction (XRD) patterns are acquired on a Bruker D8 DISCOVER with Cu Kα (λ = 1.5418Å). Powders compositions are investigated using a Thermofisher K-alpha X-ray photoelectron spectrometer (XPS), equipped with a monochromatic Al Kα source and calibrated with the adventitious carbon (C1s) peak being normalized at 285.0 eV. Bulk electronic properties are characterized by Electron Paramagnetic Resonance (EPR) with a Bruker ESP300E spectrometer operating at 9.54 GHz (X-band), with the spectra acquired at 4K using 20 mW microwave power and normalized in accordance to the mass of the sample, gain and number of accumulated scans. UV-Vis-NIR data are recorded using a Shimadzu UV-3600i Plus spectrophotometer, with the absorption of the powders being measured using an integrating sphere (ISR-1503) and exploiting the Kubelka-Munk formalism (see below) to transform diffuse reflectance measurements into absorption-proportional data. Spectroelectrochemical (SEC) characterization of the films is carried out using the same spectrophotometer (without the integrating sphere), exploiting an adapted sample holder for a three-electrode configuration (consisting in the sample itself as working electrode, an Ag/AgCl reference electrode and a Pt foil counter electrode) in an optical glass cell. The electrochemical bias is controlled with a Biologic SP-200 potentiostat/galvanostat.

Interpretation of the optical measurements: The powders are characterized in terms of optical absorption by measuring their diffuse reflectance through UV-VIS-NIR spectrophotometry, and applying the Kubelka-Munk (KM) function.[8,13,47,49] Further details on the application of the KM formalism to various plasmonic materials, including MoWOx compounds, are given and discussed in a dedicated study.[48]

Briefly, the KM formalism (**Equation 1**) correlates the diffuse reflectance of the sample R_∞ to the quotient of its absorption coefficient (k) and scattering coefficient (s):[48,50,51]

$$k/s = (1 - R_\infty)^2/2R_\infty \quad (1)$$

Since both k and s are wavelength-dependent in plasmonic materials, k cannot be deduced from a measurement of the pure powder. To resolve this issue, the sample is diluted in a white powder (LiF, in a LiF/sample ratio of 90/10) that possesses a constant diffusion coefficient and almost no absorption over the measurement interval. In these conditions, the diffusion coefficient of the mixture is constant at a value corresponding to that of the white powder, and the absorption coefficient only results from the studied material. The 10 wt. % proportion in diluting agent is selected to best fulfill the KM conditions while keeping a good signal to noise ratio. The absorption data are computed from the diffuse reflectance measurements using the KM formula, replacing the R_∞ term in the formula (Equation 1) with the reflectance of the powder measured at a given wavelength.[50,51]

Interpretation of the electrochromic characterizations: In order to quantify the optical contrasts of the films in a more precise manner, the latter are computed taking in account the average transmittance over an interval of wavelength representing the VIS (350-750 nm) and NIR ranges (750-1650 nm), rather than extracted from the difference of transmittance values at a specific single wavelength characterization. The average transmittance over a given interval is also used for the calculation of the coloration efficiency (CE, in cm^2C^{-1}) of the electrochromically active layers, determined in both VIS and NIR ranges, from the transmittance spectra and electrochemical data acquired during the SEC characterization, replacing the T_b, T_c (averaged values of transmittance in the bleached and colored states, respectively,) and Q_{in} (inserted charge per cm^2) terms accordingly in the following **Equation 2**:[40,52]

$$CE = (log\,(T_b/T_c))/Q_{in} \quad (2)$$

Finally, as a way to quantify the capacitive behavior observed in the SEC characterizations in the $TBAClO_4$/propylene carbonate electrolyte, two figures of merits are defined: the first one is the proportion of capacitive behavior in the optical contrast ($\Delta T_{capa.}$, **Equation 3**), averaged on the VIS and NIR ranges of the sample:

$$\Delta T_{capa.} = 100 * \Delta T_{TBA+}/\Delta T_{Li+} \quad (3)$$

Where ΔT_{TBA+} and ΔT_{Li+} are the optical contrasts measured in the $TBAClO_4$/propylene carbonate and $LiClO_4$/propylene carbonate electrolytes, respectively.

A second figure of merit is established to take in account the capacitive behavior in both optical and electrochemical data:

$$K = \Delta T_{capa.}/\left(100 * Q_{in,TBA+}/Q_{in,Li+}\right) \quad (4)$$

In this equation, K is a unitless factor defined as the capacitive contribution and is calculated by dividing $\Delta T_{capa.}$ by the capacitive proportion of the inserted charge (in $TBAClO_4$/PC or $LiClO_4$/PC, respectively $Q_{in,TBA+}$ and $Q_{in,Li+}$) in a given optical state (and thus at a given electrochemical bias).

Acknowledgments

The authors acknowledge the support of the FRS-F.N.R.S. under the convention PDR T.0125.30 PLASMON_EC. M.L. is a Research Associate of the Fonds de la Recherche Scientifique – FNRS. A.M. thanks U. Liège-GREEnMat for additional funding and support, as well as U. Bordeaux and ICMCB-CNRS through his "Chaire de Professeur Junior" supported by Agence Nationale de la Recherche. L.H. acknowledges fruitful discussions with Waqas Zulfiqar, Mohamed Achehboune and Daphanée Tueguem Tabwe on the electronic properties of MoWOx. Moreover, the authors warmly thank Jean-François Colomer for TEM images and the SIAM platform at the University of Namur for the XPS characterizations.

References

1. Agrawal, A., Cho, S.H., Zandi, O., Ghosh, S., Johns, R.W., Milliron, D.J. *Chem. Rev.*, **2018**, *118*, 3121.
2. Wang, Y., Runnerstrom, E.L., Milliron, D.J. *Annu. Rev. Chem. Biomol. Eng*, **2016**, *7*, 283.
3. A. Maier, S. *Plasmonics : Fundamentals and Applications*, Springer-Verlag US **2007**.
4. Runnerstrom, E.L., Llordés, A., Lounis, S.D., Milliron, D.J. *Chem. Commun.*, **2014**, *50*, 10555.
5. Tegg, L., Keast, V.J. *Plasmonics*, **2023**, *18*, 49.
6. Adachi, K., Asahi, T. *J. Mat. Res.*, **2012**, *27*, 965.
7. Wang, T., Xiong, Y., Li, R., Cai, H. *New J. Chem*, **2016**, *40*, 7476.
8. Yin, H., Kuwahara, Y., Mori, K., Cheng, H., Wen, M., Huo, Y., Yamashita, H. *J. Phys. Chem. C*, **2017**, *121*, 23531.
9. Li, P., Zhu, L., Ma, C., Zhang, L., Guo, L., Liu, Y., Ma, H., Zhao, B. *ACS Appl. Mater. Interfaces*, **2020**, *12*, 19153.
10. Zhong, X., Sun, Y., Chen, X., Zhuang, G., Li, X., Wang, J.G. *Adv. Funct. Mater.*, **2016**, *26*, 5778.
11. Zhao, Y., Tang, Q., He, B., Yang, P. *Int. J. Hydrogen Energy*, **2017**, *42*, 14534.
12. Zhang, N., Jalil, A., Wu, D., Chen, S., Liu, Y., Gao, C., Ye, W., Qi, Z., Ju, H., Wang, C., Wu, X., Song, L., Zhu, J., Xiong, Y. *J. Am. Chem. Soc.*, **2018**, *140*, 9434.
13. Xue, N., Yu, R.J., Yuan, C.Z., Xie, X., Jiang, Y.F., Zhou, H.Y., Cheang, T.Y., Xu, A.W. *RSC Adv.*, **2017**, *7*, 2351.
14. Zhang, S., Cao, S., Zhang, T., Yao, Q., Fisher, A., Lee, J.Y. *Mater. Horizons*, **2018**, *5*, 291.
15. Zhang, S., Cao, S., Zhang, T., Fisher, A., Lee, J.Y. *Energy Environ. Sci.*, **2018**, *11*, 2884.
16. Zhang, S., Li, Y., Zhang, T., Cao, S., Yao, Q., Lin, H., Ye, H., Fisher, A., Lee, J.Y. *Appl. Mater. Interfaces*, **2019**, *11*, 48062.
17. Tandon, B., Lu, H.-C., Milliron, D.J. *J. Phys. Chem. C*, **2022**, *126*, 9228.
18. Kim, J., Agrawal, A., Krieg, F., Bergerud, A., Milliron, D.J. *Nano Lett.*, **2016**, *16*, 3879.
19. Okada, M., Ono, K., Yoshio, S., Fukuyama, H., Adachi, K. *J. Am. Ceram. Soc.*, **2019**, *102*, 5386.
20. Wang, W., Janotti, A., Van De Walle, C.G. *J. Mater. Chem. C*, **2016**, *4*, 6641.
21. Deb, S.K. *Sol. Energy Mater. Sol. Cells*, **1995**, *39*, 191.
22. Yoshio, S., Adachi, K. *Mater. Res. Express*, **2018**, *6*, 026548.
23. Walkingshaw, A.D., Spaldin, N.A., Artacho, E. *Phys. Rev. B - Condens. Matter Mater. Phys.*, **2004**, *70*, 1.
24. Hassani, H., Partoens, B., Bousquet, E., Ghosez, P. *Phys. Rev. B*, **2022**, *105*, 014107.
25. Sajadi, B., Mirnaghi, M., Akhavan-Behabadi, M., Delgarm, N., Goudarzi, A. *Energy Equip. Syst.*, **2021**, *9*, 1.
26. Sheng, S.-Z., Wang, J.-L., Zhao, B., He, Z., Feng, X.-F., Shang, Q.-G., Chen, C., Pei, G., Zhou, J., Liu, J.-W., Yu, S.-H. *Nat. Commun.*, **2023**, *14*, 1.

27. Zhao, S., Wang, B., Zhu, N., Huang, Y., Wang, F., Li, R., Zhao, Y., Jiang, Q., Wu, X., Zhang, R. *Carbon Neutralization*, **2023**, *2*, 4.

28. Zhai, Y., Li, J., Shen, S., Zhu, Z., Mao, S., Xiao, X., Zhu, C., Tang, J., Lu, X., Chen, J. *Adv. Funct. Mater.*, **2022**, *1*, 2109848.

29. Barawi, M., Veramonti, G., Epifani, M., Giannuzzi, R., Sibillano, T., Giannini, C., Rougier, A., Manca, M. *J. Mater. Chem. A*, **2018**, *6*, 10201.

30. Dahlman, C.J., Tan, Y., Marcus, M.A., and Milliron, D.J. *J. Am. Chem. Soc.*, **2015**, *137*, 9160.

31. Yilmaz, P., Magni, M., Martinez, S., Maria Gonzalez Gil, R., Della Pirriera, M., Manca, M. *ACS Appl. Energy Mater*, **2020**, *3*, 3779.

32. Zhou, D., Shi, F., Xie, D., Wang, D.H., Xia, X.H., Wang, X.L., Gu, C.D., Tu, J.P. *J. Colloid Interface Sci.*, **2016**, *465*, 112.

33. Lagier, M., Bertinotti, A., Bouvard, O., Burnier, L., Schüler, A. *Opt. Mater.*, **2021**, *117*, 111091.

34. Arvizu, M.A., Niklasson, G.A., Granqvist, C.G. *Chem. Mater.*, **2017**, *29*, 2246.

35. Xie, S., Bi, Z., Chen, Y., He, X., Guo, X., Gao, X., Li, X. *Appl. Surf. Sci.*, **2018**, *459*, 774.

36. De León, J.M.O.R., Acosta, D.R., Pal, U., Castañeda, L. *Electrochim. Acta*, **2011**, *56*, 2599.

37. Wang, B., Man, W., Yu, H., Li, Y., Zheng, F. *Materials*, **2018**, *11*, 1627.

38. Kumar, A., Chandra Prajapati, S., Sahay, P.P. *J. Sol-Gel Sci. Technol.*, **2019**, *90*, 281.

39. Li, W., Zhang, J., Zheng, Y., Cui, Y. *Sol. Energy Mater. Sol. Cells*, **2022**, *235*, 111488.

40. Li, H., Chen, J., Cui, M., Cai, G., Eh, A.L.S., Lee, P.S., Wang, H., Zhang, Q., Li, Y. *J. Mater. Chem. C*, **2015**, *4*, 33.

41. Li, H., Li, J., Hou, C., Ho, D., Zhang, Q., Li, Y., Wang, H. *Adv. Mater. Technol.*, **2017**, *2*, 1700047.

42. Li, H., Mcrae, L., and Elezzabi, A.Y. *Appl. Mater. Interfaces*, **2018**, *10*, 10520.

43. Zhou, L., Zhu, J., Yu, M., Huang, X., Li, Z., Wang, Y., Yu, C. *J. Phys. Chem. C*, **2010**, *114*, 20947.

44. Arzola-Rubio, A., Camarillo-Cisneros, J., Fuentes-Cobas, L., Collins-Martínez, V., De La Torre-Sáenz, L., Paraguay-Delgado, F. *Superlattices Microstruct.*, **2015**, *81*, 175.

45. Li, H., McRae, L., Firby, C.J., Al-Hussein, M., Elezzabi, A.Y. *Nano Energy*, **2018**, *47*, 130.

46. Wang, Q., Li, C., Xu, W., Zhao, X., Zhu, J., Jiang, H., Kang, L., Zhao, Z. *Appl. Surf. Sci.*, **2017**, *399*, 41.

47. Yin, H., Kuwahara, Y., Mori, K., Yamashita, H. *J. Mater. Chem. A*, **2018**, *6*, 10932.

48. Lobet, M., Gillissen, F., Demoor, N., Dewalque, J., Colson, P., Cloots, R., Maho, A., Henrard, L. *(Preprint) arXiv:*2406.02181, v1, submitted: Jun **2024**. https://arxiv.org/abs/2406.02181

49. Kuwahara, Y., Yoshimura, Y., Haematsu, K., Yamashita, H. *J. Am. Chem. Soc.*, **2018**, *140*, 9203.

50. Kubelka, P., and Munk, F. *Zeit. Für Tekn. Phys.*, **1931**, *12*, 593.

51. Kortüm, G. *Reflectance Spectroscopy: Principles, Methods, Applications*, Springer-Verlag, Berlin-Heidelberg, **1969**.

52. Granqvist, C.G. *Electrochim. Acta*, **1999**, *44*, 3005.

53. Machida, K., Adachi, K. *J. Phys. Chem. C*, **2016**, *120*, 16919.

54. Huang, X., El-Sayed, M.A. *J. Adv. Res.*, **2010**, *1*, 13.

55. Mogensen, K.B., Kneipp, K. *J. Phys. Chem. C*, **2014**, *118*, 28075.

56. Triana, C.A., Granqvist, C.G., Niklasson, G.A. *J. Appl. Phys.*, **2015**, *118*, 024901.

57. Sarr, M., Bahlawane, N., Arl, D., Dossot, M., Mcrae, E., Lenoble, D. *Appl. Surf. Sci.*, **2016**, *379*, 523.

58. Chow, W.K., So, C.M., Lau, C.P., Kwong, F.Y. *Org. Chem. Front.*, **2014**, *1*, 464.

59. Dominguez, J.E., Fu, L, Pan, X. Q. *J. Appl. Phys.*, **2002**, *81*, 5168.

60. Ahmed, N.M., Sabah, F.A., Abdulgafour, H.I., Alsadig, A., Sulieman, A., Alkhoaryef, M. *Results Phys.*, **2019**, *13*, 102159.

61. Patil, P., Patil, P. *Thin Solid Films*, **2001**, *382*, 13.

62. Yin, H., Kuwahara, Y., Mori, K., Louis, C., Yamashita, H. *Catal. Sci. Technol.*, **2020**, *13*, 4141.

63. Idriss, H. *Surf. Sci.*, **2021**, *712*, 2.

64. Manthiram, K., Alivisatos, A.P. *J. Am. Chem. Soc*, **2012**, *134*, 3995.

65. Runnerstrom, E.L. *PhD Thesis*, University of California, Berkeley **2016**.

66. Salje, E., Güttler, B. *Philos. Mag. B*, **1984**, *50*, 607.

67. Zhou, H., Zou, X., Zhang, K., Sun, P., Islam, M.S., Gong, J., Zhang, Y., Yang, J. *Appl. Mater. Interfaces*, **2017**, *9*, 18669.

68. Inamdar, A.I., Chavan, H.S., Talha, A., Ahmed, A., Cho, S., Kim, J., Jo, Y., Pawar, S.M., Park, Y., Kim, H., Im, H. *Mater. Lett.*, **2018**, *215*, 233.

69. Lu, X., Zeng, Y., Yu, M., Zhai, T., Liang, C., Xie, S., Balogun, M.S., Tong, Y. *Adv. Mater.*, **2014**, *26*, 3148.

70. El-Habib, A., Addou, M., Aouni, A., Diani, M., Nouneh, K., Zimou, J., Marjaoui, A., Barbouch, Z., Zanouni, M., El Jouad, Z. *Opt. Mater.*, **2022**, *127*, 112312.

71. Tran, N., Croguennec, L., Ménétrier, M., Weill, F., Biensan, P., Jordy, C., Delmas, C. *Chem. Mater.*, **2008**, *20*, 4815.

72. Ohsaka, T., Kanzaki, Y., and Abe, M. *Mater. Res. Bull.*, **2001**, *36*, 2141.

73. Pérez-Flores, J.C., Baehtz, C., Hoelzel, M., Kuhn, A., García-Alvarado, F. *RSC Adv.*, **2012**, *2*, 3530.

74. Jouanneau, S., Sarciaux, S., Le Gal La Salle, A., Guyomard, D. *Solid State Ionics*, **2001**, *140*, 223.

75. Bondarenko, N., Eriksson, O., and Skorodumova, N. V. *Phys. Rev. B - Condens. Matter Mater. Phys.*, **2015**, *92*, 165119.

76. Maho, A., Nayak, S., Gillissen, F., Cloots, R., Rougier, A. *Coatings*, **2023**, *13*, 1.